Lab on a Chip

Soil granular dynamics on-a-chip: fluidization inception under scrutiny

Journal:	*Lab on a Chip*
Manuscript ID	LC-ART-12-2018-001376.R1
Article Type:	Paper
Date Submitted by the Author:	09-Feb-2019
Complete List of Authors:	Houssais, Morgane; City College of CUNY, Levich Institute; Maldarelli, Charles; City College of CUNY, Levich Institute/Chemical Engineering Morris, Jeffrey; City College of CUNY, Levich Institute/Chemical Engineering

Cite this: DOI: 00.0000/xxxxxxxxxx

Soil granular dynamics on-a-chip: fluidization inception under scrutiny

Morgane Houssais,*[a], Charles Maldarelli[b] and Jeffrey F. Morris[b]

Received Date
Accepted Date

DOI: 00.0000/xxxxxxxxxx

Predicting soil evolution remains a scientific challenge. This process involves poorly understood aspects of disordered granular matter and dense suspension dynamics. This study presents a novel two-dimensional experiment on a small-scale chip structure; this allows the observation of the deformation at the particle scale of a large-grained sediment bed, under conditions where friction dominates over cohesive and thermal forces, and with an imposed fluid flow. Experiments are performed at conditions which span the particle resuspension criterion, and particle motion is detected and analyzed. The void size population and statistics of particle trajectories bring insight to the sediment dynamics near fluidization conditions. Specifically, particle rearrangement and net bed compaction are observed at flow rates significantly below the criterion for instability growth. Above a threshold, a large vertical channel through the bed forms. In the range of flow rates where channelization can occur, the coexistence of compacting and dilating bed scenarios is observed. The results of the study enhance our capacity for modeling of both slow dynamics and eventual rapid destabilization of sediment beds. Microfluidic channel soil-on-a-chip studies open avenues to new investigations including dissolution-precipitation, fine particle transport, or micro-organism swimming and population growth, which may depend on mechanics of the porous medium itself.

1 Introduction

Soils are the fine layer of disordered matter, made of inorganic and organic particles, on which relies most life on the continents. Composition of soils varies widely, and these are complex systems where many physical, chemical, and biological phenomena take place. The processes involve a wide range of spatial scales, from the typical soil thickness of O(1) m, to $O(10^{-8})$ m which is the scale of the smaller particles and voids, to $O(10^{-9})$ m which is the scale of chemical and bio-chemical processes. Microfluidics is a natural and emerging approach to study fluid and particle transport processes in soils on the particle or pore scale, particularly for granular media with particles of the order of 10^{-6} to 10^{-3} m in size[1–3]. Most studies have used microfluidics to model a static simplified version of a sedimented porous medium, in order to focus on the dynamics inside its voids. This neglects the dynamics of the particles making up the porous medium, although it is known that soils change and deform. These motions may occur slowly through creep down a slope and weathering processes, or they may occur quickly when any sort of liquefaction or fluidization takes place[4,5]. In this regard, a number of macroscopic experimental studies have been conducted to determine the bulk mechanical response of soils of many different compositions and water contents under varying applied stress[6,7]. While these bulk studies display the collective particle dynamics, much of the behavior on the particle scale remains unresolved. Recent studies on the dynamics of dense suspensions of particles under simple shear demonstrate the complexity of fluid-particle interactions that are relevant to the motion of sediments. These studies have shown that under stress two populations of contact, lubricated and frictional, can develop and build into two intricate and history dependent structural networks[8–12].

Our interest here is in using microfluidics to understand, on the local pore scale, the process of fluidization or channelization, in gravity-loaded particle beds with a free surface and subject to a vertical upward fluid flow. It has been shown that even when air is injected through a single horizontal layer of dry particles, their collective dynamics exhibits a solid-fluid transition with decrease of the packing fraction[13]. It has also been observed that the dynamics of liquid flowing horizontally through a particulate system is highly sensitive to any local change of pressure, due to void size heterogeneity or free surface (the upper surface where solid fraction drops suddenly) curvature, the latter of which may result from local erosional deposition of particles[14,15]. Consequently,

[a] Levich Institute, City College of CUNY, 140th Street and Convent Avenue, New York, NY 10031, USA. Fax: XX XXXX XXXX; Tel: XX XXXX XXXX; E-mail: housais.morgane@gmail.com
[b] Levich Institute and Chemical Engineering Department, City College of CUNY, 140th Street and Convent Avenue, New York, NY 10031, USA.

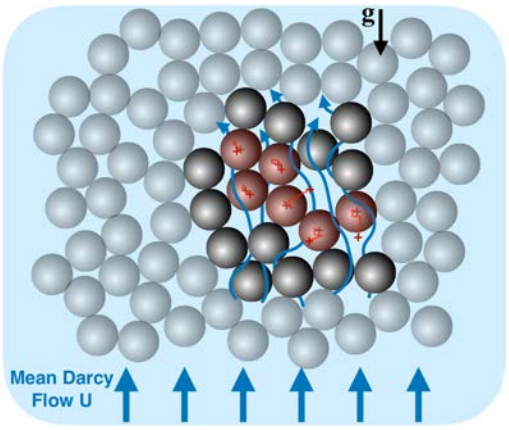

Fig. 1 Dynamics sketch. Porous flow through a disordered frictional material triggering a particles collective rearrangement under gravity. Fine blue arrows represent local fluid flow field. Crosses indicate particles position, before (gray) and after (red) the collective event.

predicting such phenomena as the inception of local fluidization of a sediment bed – generally jammed at rest and with a free surface – remains highly challenging.

Figure 1 illustrates schematically the pore-scale liquid flow through a porous medium made of particles. The system remains fully jammed, until the resultant of contact (including frictional) forces at particle contacts, and the drag force on particles determined by the local flow configuration result in particle rearrangement, whether individually or collectively. Under gravity, as long as such rearrangement induces no significant change of the local liquid flow field, the system energy will then find another local minimum. However, if a particular void grows significantly in a rearrangement, a coupled hydrodynamic-mechanical instability may take place as the liquid flow strengthens in that void. If flow strengthens sufficiently to counteract particle settling, local re-suspension of particles occurs and the cavity can maintain itself and grow into a channel. When the channel grows long enough that it crosses the entire bed, a chimney state is reached.

Often motivated by modeling of fluidization in industrial silo designs, a body of experimental work has been conducted on the onset of localized fluidization by a vertical flow point source [16–19]; dynamics of particles in the vicinity of channel inception is not well-reported as it is difficult to observe. Philippe and Badiane [18], using refractive index matching techniques, were recently able to capture the growth of a cavity into a channel and then a chimney. This was achieved in a three-dimensional (3D) experiment where flow is injected from a small orifice in a submerged settled granular bed. Interestingly, this group quantified from direct measurement of the cavity geometry the existence of a well-known hysteretic behavior: as the flow discharge through the orifice increased, the system remained quasi-static under the internal stresses generated by the porous flow until it reached a critical discharge value where the system evolved rapidly to a chimney state. When the flow discharge was decreased from a fully channelized state to the original low discharge value (which was unable to initiate the channelization), the persistence of a cavity was observed.

Although it is clear that a mechanical instability is responsible for the cavity growth, part of the hysteretic behavior remains to be understood. In particular, closer attention to the granular system structure such as the packing fraction, or perhaps better the population of voids, seems to be required to improve understanding of the dynamical context in which the inception and growth of local re-suspension takes place. Finally, for those interested in the dynamics and eventual destabilization of large (often modeled as semi-infinite) systems such as soils, imposing a homogeneous flow appears to be more relevant than point source injection for study of the system near instability.

In this study, we present results from a novel microfluidic experiment, where rigid and athermal particles form a wide frictional sediment bed in a channel, close to being purely two-dimensional (2D), lying on a horizontal grid. The channel design allows us to impose homogeneous liquid flow at the base of the bed, and does not fix the position where a cavity can grow. Using fine control of the fluid flow through the whole system, combined with detection of individual particle motions and void sizes between the particles, we investigate the inception of local fluidization. The quasi-2D geometry allows accurate and detailed measurements over the entire bed, and as a result, the study provides quantitative and new insights to the system dynamics in the vicinity of the onset of channelization. Local and bulk deformation measurements verify previous observations. These measurements also shed new light on how slow sub-critical particle rearrangement, or creep, can result from the combination of gravity and porous flow stresses, and how the accumulated effects over long times can impact the global system dynamics.

2 Experimental setup and protocol

2.1 Microfluidics setup

Experiments are performed in a channel of Hele-Shaw type, of dimensions $L_x = 6.7$ cm, $L_z = 2.5$ cm and depth $L_y = \delta = 500$ μm, always filled with water, at room temperature room, of density $\rho = 1000$ kg.m^{-3} and viscosity $\eta = 0.001$ Pa.s. A fixed volume fraction (0.2 % of water volume) of soap is added, in order to prevent particle-particle cohesion caused by air bubbles. The channel is positioned such that the z axis is vertical, parallel to gravity, such that a sediment bed of heavy particles can form at the bottom (see sketch and photograph in figure 2). The sediment is made of polystyrene spherical particles of mean diameter $d = 400$ μm and density $\rho_p = 1050$ kg.m^{-3} and rests on a grid, made of pylons, designed for this purpose. The particle size distribution is narrow, in order for particles to settle freely in the near-2D configuration, as shown in figure 2b, while allowing all voids and particles to be detectable by image analysis; examples of captured images are shown in figure 2c and figure 3). At the bottom of the channel, under the grid, water is injected by a syringe pump, through a 1.5 mm diameter tube. A vertical distance of 2 cm separates the injection source from the bed, and the last 5 mm is filled by 0.5 mm posts. The posts laterally homogenize the flow, and prevent particles from falling near the injection source. The lateral sides of the channel (not visible on photographs) were designed, using half pylons, to be bumpy, so that the particles interact with a solid

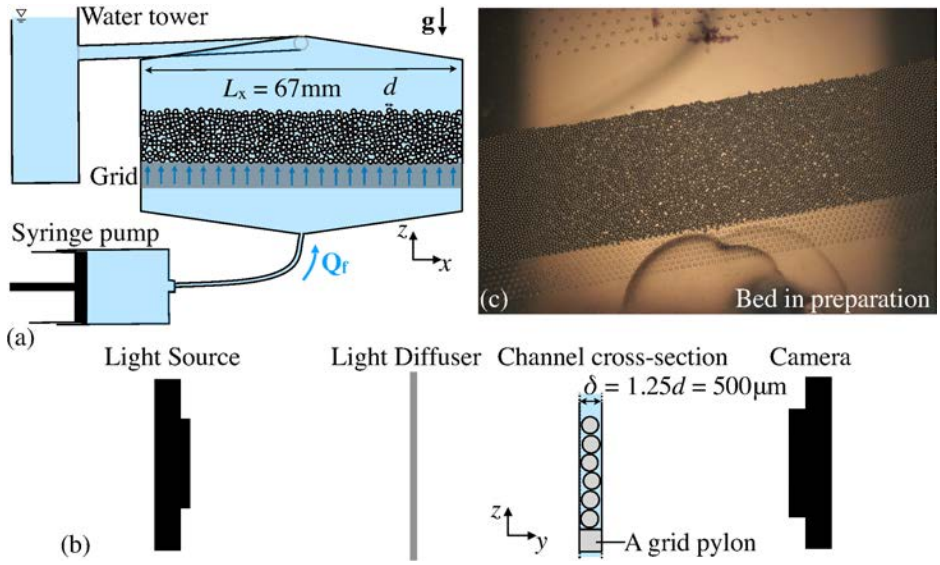

Fig. 2 Sketches of (a) the microfluidics channel experiment (particles not represented at their real size relative to the channel width L_x), and (b) the side view of the experimental setup (where particles are scaled relative to the channel depth δ). (c) Example of raw image taken at the end of bed preparation (using a setup angle $\theta > 0$). All experiments results discussed in this paper, were performed at $\theta = 0^o \pm 0.3^o$.

surface with a geometry matching that of the grid surface.

The channel is made of two PDMS slices, with one side etched with the channel geometry using classical photolithography techniques[20]. However, in order to have very good flatness and constant depth of the channel, the mold master was made using SUEX pre-made 500 μm sheets of 96 mm diameter (from DJ MicroLaminates, Inc). The sheet was laminated onto a wafer, using heat- and speed-controlled Sky 335R6 Laminator. To assemble the two PDMS slices, their surfaces were first treated with a plasma cleaner, and they were baked once assembled. Finally, before being filled, the channel interior walls were oxidized and silanized with polyetheylene glycol (PEG), in order to make them hydrophilic[21]; this prevents bubbles and particles from sticking to the channel walls. Bubbles that enter during the bed preparation can thus be removed by gentle tapping of the channel.

Finally, the upper tubing of the channel is connected to a fixed water tower, which assures a constant hydrostatic pressure at the channel center, independent of the rate of upward flow discharge (see figure 2a and Supplementary Information).

2.2 Bed preparation

Particle filling of the channel is achieved by slowly pouring a suspension into a funnel pre-filled with water. The 4 mm outlet of the funnel is placed in the upper hole entering the channel, which is itself filled with water. This upper hole has diameter ten times that of the particles, in order to prevent jamming while pouring the suspended particles through the hole[22,23]. This technique allows the particles to gently settle down the funnel into the channel and then into the channel. The channel itself is kept at an angle with the horizontal, for particles to settle further down onto the channel grid.

Before each experiment, the sediment bed was prepared by the following sequence of steps: 1) At setup angle $\theta = 0^o$, water flow was injected from below, at a rate sufficient to re-suspend all of the particles. 2) While the particles were in suspension, the angle was changed to $+15^o$, so that particles settled down toward one end of the channel. 3) The angle was changed to -15^o, and an upward flow discharge of 215 μL/min was imposed, in order to trigger a slow particle flow down the slope, flattening the bed and making the bed surface parallel to the grid after 2 to 5 min. 4) The setup angle was then returned to $\theta = 0^o$, and the bed was weakly re-suspended again by a short manual injection, which displaced the particles just a few millimeters above the grid. This step has the goal of removing structural anisotropy that may have developed in the preceding steps, thus enhancing the randomness of the porous media. 5) Immediately after particle settling in step 4, a suspended mass (of 300 g) was used to "tap" the channel just once on the side, to compact the bed. 6) The system was let age for 5 min.

Fixing an aging period much longer than the system settling time t_s – time for a single particle to fall at Stokes velocity over its own diameter, about 0.1 second – insured that all frictional contacts are set before starting. As a result, the experiments are more reproducible.

The volume of particles was not varied, and thus the initial bed thickness was also essentially the same for each experiment.

2.3 Experiment protocol and visualization

Each experiment followed the same protocol (see figure 3a). Denote time at onset of flow by t_0. For a time Δt of 18 to 20 min, the upward flow discharge Q_f was set to a constant value. At $t_0 + \Delta t$ the discharge rate was increased for Δt_f = 2 min to the fixed value of $Q_f = 315$ μL/min, strong enough to systematically create a chimney. At $t_0 + \Delta t + \Delta t_f$, the flow was set back to the same constant value $Q_f < 315$ μL/min. Finally, at $t_0 + 2\Delta t + \Delta t_f$ the upward flow was stopped and settling was allowed for 2 m in. Images of 5184×3456 pxl were taken (Canon EOS rebel t3i camera) during the whole procedure, at 0.25 fps (1 frame every 4 s) from t_0 to

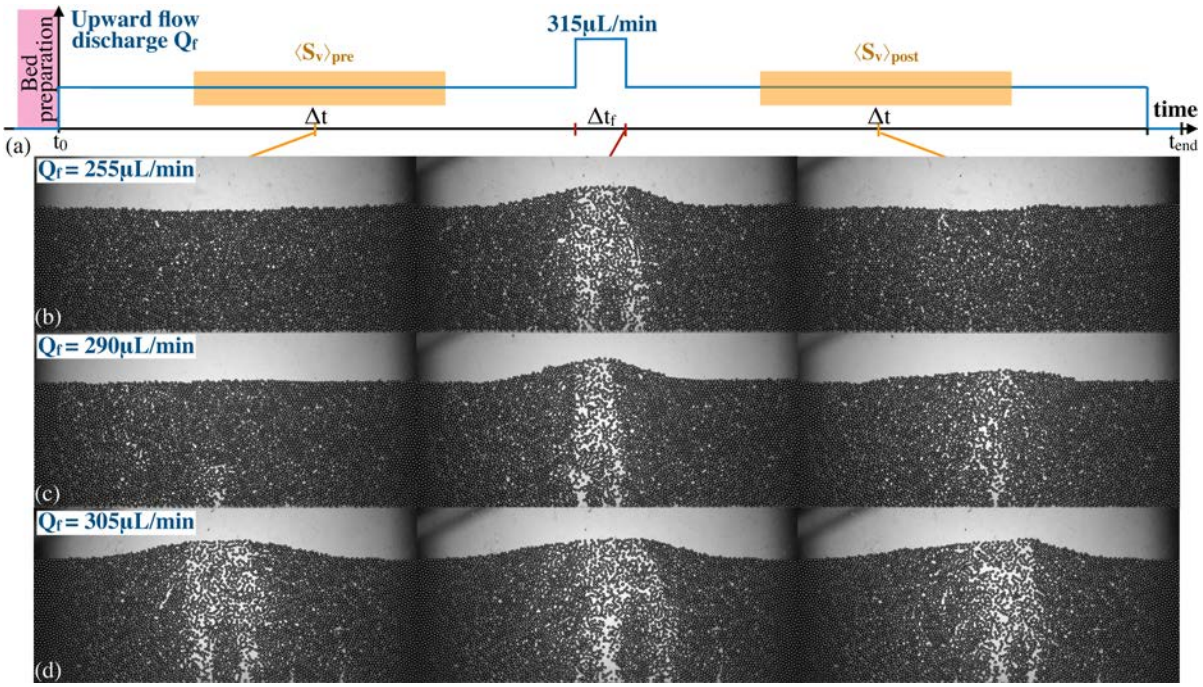

Fig. 3 Fluidization experimental protocol. (a): sketch of the fluidization experiment protocol. Images from top to bottom: from left to right, pictures captured respectively at $t_0+\Delta t/2$, $t_0+\Delta t+\Delta t_f$ and $t_0+\Delta t+\Delta t_f+\Delta t/2$, and for upward flow discharge Q_f equal to (b) 255, (c)290 and (d) 305 μL/min.

t_0+5 min, from $t_0+\Delta t$ to $t_0+\Delta t+\Delta t_f$ and from $t_0+\Delta t+\Delta t_f$ to $t_0+\Delta t+\Delta t_f+5$ min. For the remainder of the experiment, images were recorded at 0.036 fps (1 frame every 28 s). The image resolution is, on average, 28 pxl per particle diameter, or 0.014 mm/pxl, and $\pi(d/2)^2 = 0.139$ mm$^2 \simeq 616$ pxl^2. As the system is nearly 2D and illuminated from the back with a controlled light source, all particles are visible on images over the region covered by a square light diffuser of 4 inches on a side. Finally, the fluid injection was controlled via a Harvard PHD2000 syringe pump, which was remote controlled and timed with the camera, using a single python script which calls for gPhoto free software and the Pumpy python module.

2.4 Image analysis

Images are analyzed to extract statistical information on the voids at each sampling instant. During periods of slow reorganization (sub-critical conditions), particle trajectories are computed and analyzed using OpenCV and common python libraries. Each image is first binarized using local thresholding, with particle centers identified as bright objects of circular shape within a size range. The particles are tracked using trackpy[24]. Subsequent treatment makes the bright particle centers dark, in order to have only the voids left bright. From this modified version of the images, the bed surface is measured as the largest object contour in the system, and voids are detected below the bed surface.

3 Results

3.1 Void size distribution

Figure 4a illustrates typical void detection results with magenta crosses showing detected void centers, while 4b shows typical results of distributions of void sizes (areas) detected, for a few images. Darker curves represent earlier bed states, and lighter ones later states, until the end of the middle stage of the experiment, at $t = t_0+\Delta t+\Delta t_f$; this specific time is represented by the green curve. One can notice two peaks, which are always present in the void size distributions, and are found spatially over the entire domain (see Supplementary Material). The first peak of the normalized void size ($S_v/\pi(d/2)^2$) distribution has a mean value close to 0.12 and is followed by a local minimum, and then by a second, and broader, peak starting at about 0.28. Those two specific values are consistent with the smaller void size one can find in a purely 2D system – the space between three disks or coplanar spheres in contact – which is exactly $\pi(d/2)^2(2/\pi-1/2) \simeq 0.137\pi(d/2)^2$, and double this value $\simeq 0.27\pi(d/2)^2$. Slightly different values from our detection are mostly due to the fact that our system is not perfectly 2D, and to limited image resolution. The second peak of the distribution of $S_v/\pi(d/2)^2$ is wider, around a mean value which is generally close to 0.4 at t_0, and often becomes wider during an experiment; this value is consistent with the merging, of a void between three disks and a void between four disks $\simeq (2+1)*0.137\pi(d/2)^2 \simeq 0.41\pi(d/2)^2$. The largest value of S_v associated with the second peak appears to be marked by the merging of a 4-disk void and another 3-disk void ($\simeq (3+1)*0.137\pi(d/2)^2 \simeq 0.55\pi(d/2)^2$). If that merging resulted in a regular pentagon, the corresponding maximum would be $\simeq 0.69\pi(d/2)^2$. After this second peak ending at the regular pentagon void value, the distribution of void sizes is roughly an exponential decay until $S_v/\pi(d/2)^2 \simeq 3$. As the fluidization of the system takes place, we can observe some change in the distribution peaks, but no significant change of the overall shape of the distribution.

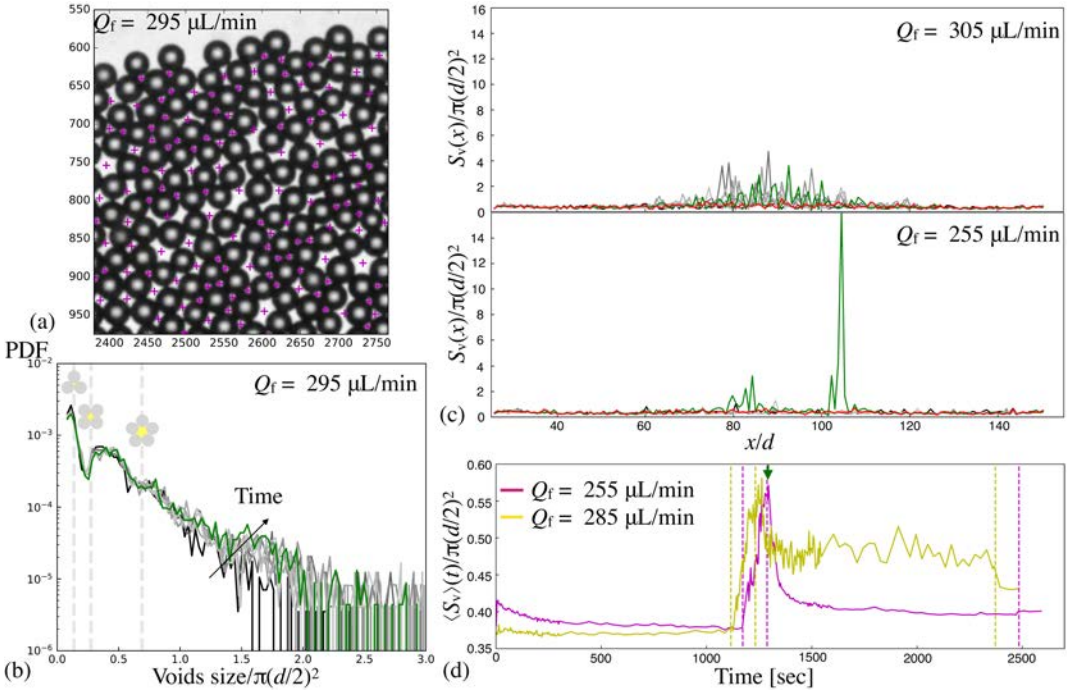

Fig. 4 Void size detection. (a) Raw image sample (axes in pixels), captured during an experiment, with superimposed on this the detected bed surface (green curve) and void center positions (blue crosses). (b) Probability distribution function of detected void area, normalized by the average projected particle area, during an experiment performed under $Q_f = 295$ μL/min (from which the image above is extracted). (c) Averaged values of normalized void size over the bottom 2/3 of the bed as a function of the horizontal position in the bed. Levels of gray represent time during the experiment, with lighter lines at later time. (d) Two examples of the time evolution of the spatially-averaged void size $\langle S_v\rangle(t)$.

Figure 4c shows the horizontal distribution of the mean void size, averaged over the bottom two thirds of the bed, and its evolution during an experiment, from t_0 to $t_0 + \Delta t + \Delta t_f$. Data are shown for the two experiments represented on figure 3 , for flow discharges resulting in significantly different sediment bed dynamics. The green line represents the void sizes at $t_0 + \Delta t + \Delta t_f$, just at the end of the short increase of flow rate. The red line represents the final stage of the experiment at $t = t_{\text{end}}$. To quantify the observations as a bulk effect, we estimate the space-averaged value $\langle S_v\rangle$ as the average of the profiles over x, and do so for all the voids detected in the bed from $x/d = 40$ to $x/d = 140$, about $60d$ from the side walls. Figure 4d shows a typical time evolution for the experiment performed at $Q_f = 255$ and 285 μL/min. On those curves one can readily observe the three phases of the experiment under or near the fluidization criterion: the bed exhibits compaction during the first phase, then clear dilation during the imposed channelization phase at the middle of the experiment, and finally, the maintenance of higher averaged void size, as the part of the bed which was fluidized settles back closer to a random loose packing, or due to the remaining presence of a chimney. Thus, our analysis not only recovers the classical observation of hysteretic behavior near fluidization, due to the hydro-mechanical instability leading to growth into a chimney, but also brings new observations through the details of the small time bed evolution at flow rates below that at which the instability occurs.

3.2 Dispersion of particle lateral displacement

Particle center positions, (x_i, y_i) for particles $i, \ldots, N$, are detected in each image, and tracked over time. Given that no slope is imposed and the channel bottom is flat, in this regime of imposed porous flow, the average x displacement is zero. As net compaction or dilation occurs during the experiment, we analyze the standard deviation of lateral displacement, σ_x, which serves as a measure of the disturbance by the flow, before it reaches the criterion for channelization. We measure this quantity for all experiments performed at flows under 280 μL/min in the first phase of the experiment, from t_0 to $t_0 + 15$ min.

Figure 5 presents the spatial variation of the square of the standard deviation of individual particle displacement in the x direction, normalized by measurement duration, for four runs at different mean porous flow conditions. All are obtained at flow rates below the onset of channelization. The particle positions, x_i and y_i for particles $i, \ldots, N$, are the averaged positions measured from the time window of 15 min. Over that specific time window, from $Q_f = 0$ to $Q_f = 100$ μL/min, most of the particle displacements are under our limit of detection, namely $\sigma_x(x_i, y_i) \leq 0.68$ pxl $\simeq 14\mu$m, which corresponds to an effective diffusivity below $6.3.10^{-6}$ mm^2/min. Observations under this limit correspond to the darkest blue on the figure. On figure 5b, c and d, for experiments at higher Q_f, we observe heterogeneous increase of particle lateral displacement, localized in certain regions of the bed which are adjacent to regions remaining under our detection limit. Importantly, even the highest measurements of 2.10^{-4} mm^2/min, represent only an effective diffusion of only 1.5% of

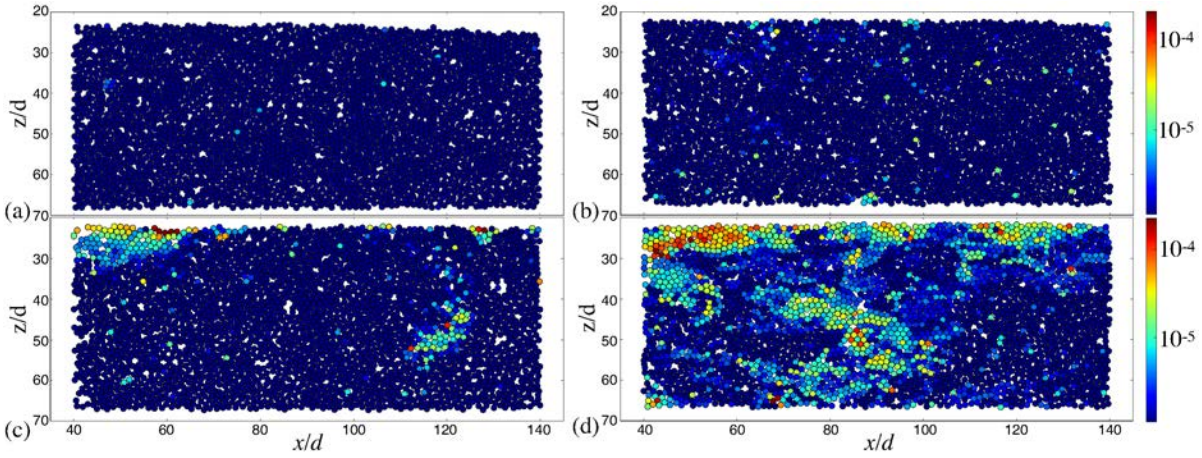

Fig. 5 Spatial distribution of the standard deviation of particles lateral motion, in mm^2/min. $\sigma_x^2/dt(x_i,y_i)$, measured over $dt = 15$ min of the 1st stage of the experiment, for four cases of (a) $Q_f = 100$ μL/min (or $P_{\text{drag}}/P_0 = 0.0225$), (b) $Q_f = 220$ μL/min (or $P_{\text{drag}}/P_0 = 0.0495$), (c) $Q_f = 245$ μL/min (or $P_{\text{drag}}/P_0 = 0.0555$), and (d) $Q_f = 265$ μL/min (or $P_{\text{drag}}/P_0 = 0.060$).

a particle's projected area per minute (one minute being about $600t_s$, with t_s the characteristic settling time noted above). Finally, we regularly observe that a few individual particles have a significantly higher diffusion, indicating these are likely rattlers, which are unconstrained by frictional contacts and thus are free to be displaced slightly more by the fluid flow.

3.3 Average void size: time evolution

Figure 6 shows the time evolution of the mean void size over the entire measured bed section, $\langle S_v\rangle(t)$, for experiments performed at six values of flow rate, from $Q_f = 255$ μL/min to $Q_f = 310$ μL/min. Colors represent different realizations of the same experiment, each made after repeating the bed preparation protocol. For flow rates up to $Q_f = 285$ μL/min, we see a systematic decrease of the mean void size with time during the first phase of the experiment, followed by an increase during the mid-experiment channelization flow at $Q_f = 315$ μL/min (delimited by vertical dashed lines). During the pre- and post-channelization stages of the experiments, the trend of the void size decay with time appears to be an exponential relaxation toward either a constant value, or a second exponential trend (see figure 6 inserts).

Importantly, the curves drop after the third vertical dashed line – marking the arrest time of the pump – on the right of each plot, indicating the presence of fast relaxation after the porous flow is stopped. For flow rates above $Q_f = 285$ μL/min, a systematic drop is observed, marking the presence of one or several highly porous areas in the bed, maintained by the local flow stresses. We use that observation as an unambiguous indicator of the presence of at least one significant cavity in the second phase of the experiment.

From these observations, one can notice three ranges of bulk flow discharge Q_f. The lower range is $0 < Q_f \leq 275$ μL/min, in which fluid flow stresses are never strong enough to initiate the growth or maintenance of a cavity; the higher range is $Q_f \geq 305$ μL/min, for which the flow is always able to do so. In the intermediate range, $275 < Q_f < 305$ μL/min, the system behavior is near critical, and is found to be hysteretic and very history dependent. In this intermediate range, experimental reproducibility is poor.

3.4 Time-averaged results

As an alternative to dependence simply on Q_f, we compute a representative pressure drop resulting from drag at the initial condition, where the bed packing fraction is spatially homogeneous:

$$P_{\text{drag}} = \frac{3\eta U_{\text{bed}}}{d} \propto \frac{F_{\text{drag}}}{4\pi(d/2)^2}\,, \qquad (1)$$

with the initial mean flow velocity inside the bed $U_{bed} = Q_f/[(1 - \langle\Phi_0\rangle)\delta\, L_x]$, with $\langle\Phi_0\rangle = 0.70$, the initial packing fraction value found (from image analysis) from averaging over all experiments. The variance of Φ_0 over all experiments is 0.01. U_{bed} itself ranges in our experiments from 0 to 0.5 mm/sec, and the average ini-tial permeability can be assessed as $(1-\Phi_0)^3 d^2/(180\Phi_0^2)$, ranging from 3.7 to 6.3 $\times$ 10^{-11} m^2. P_{drag} is normalized by the normal stress due to the particle weight, $P_0 = \alpha(\rho_p - \rho)gd/3$, with $\alpha = 1$ for the sake of simplicity, although previous studies have argued for effective α values significantly lower than unity when used to characterize the onset of fluidization[25,26].

From results presented in figures 5 and 6, we extract different mean values for each experimental realization. From the observations of void size evolution with time, we compute $\langle S_v\rangle_{\text{pre}}$ and $\langle S_v\rangle_{\text{post}}$ as the time-averaged values of $\langle S_v\rangle(t)$ computed over the time windows $[t_0 + \frac{1}{4}\Delta t, t_0 + \frac{3}{4}\Delta t]$ and $[t_0 + (1+\frac{1}{4})\Delta t + \Delta t_f, t_0 + (1+\frac{3}{4})\Delta t + \Delta t_f]$, represented in gold on figure 3 . $\langle S_v\rangle_{\text{end}}$ is the final measurement of $\langle S_v\rangle$, at $t = t_{\text{end}}$. Finally, $\Delta\langle S_v\rangle_{\text{pre}}$ and $\Delta\langle S_v\rangle_{\text{post}}$ are the total changes of $\langle S_v\rangle$ over the first 1 000 seconds, during the pre- and post- stages of the experiments, respectively.

Figure 7a presents the evolution of the mean void size as a function of the flow strength. For each flow condition, three to five realizations were performed and analyzed, except for two higher flow conditions (presented figure 6), where only two realizations were performed.

It is remarkable that for flow rates below $Q_f = 180$ μL/min ($P_{\text{drag}}/P_0 \simeq 0.04$), no significant compaction nor dilation (green

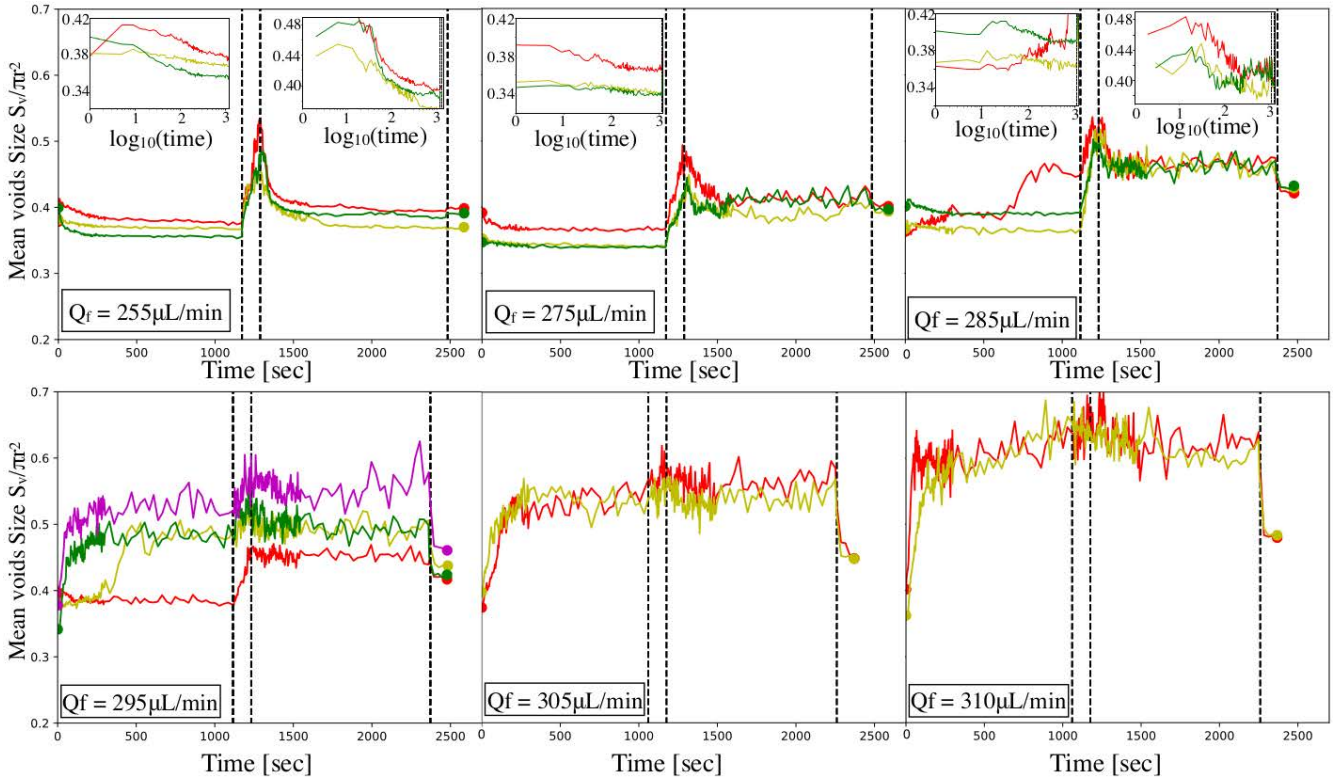

Fig. 6 Hysteresis observation, from experiments crossing the threshold for fluidization. Mean void size evolution for constant flow rate, before and after subjecting the system to a fluidizing flow rate of $Q_f = 315$ µL/min. Colors are for different realizations, for the same flow rate Q_f value. Three vertical lines on each plot respectively mark $t = t_0 + \Delta t$, $t = t_0 + \Delta t + \Delta t_f$ and $t = t_0 + 2\Delta t + \Delta t_f$. Inserts present the same data, for different pre- and post-stages, respectively in term of $log_{10}(t - t0)$ and $log_{10}(t - t_0 - \Delta t - \Delta t_f)$.

and magenta squares are on zero) can be observed during either stage of the experiments. The average void size during the post stage (represented by the yellow squares) becomes closer and closer to the initial bed preparation (represented by the thick gray dash line) as the porous flow strengthens, indicating that the channelized region is not settling to a random loose configuration as it does at $Q_f = 0$. One can observe net compaction happening from $Q_f = 180$ µL/min ($P_{\text{drag}}/P_0 \simeq 0.04$) until $Q_f = 295$ µL/min ($P_{\text{drag}}/P_0 \simeq 0.065$). In that same range, before compaction stops happening, from $Q_f = 280$ µL/min ($P_{\text{drag}}/P_0 \simeq 0.062$), some experimental runs exhibit net dilation instead. Eventually all of them exhibit dilation, at initial flows above the point of $P_{\text{drag}}/P_0 \simeq 0.065$. The coexistence of completely different scenarios – net compaction or dilation – is striking, and an indicator of near-criticality in sediment bed systems. This will be discussed further in the next section. We mark the beginning of the regime where porous flow stresses are strong enough to maintain some fraction of the particles suspended in the bed during the second phase as the point where $\langle S_v \rangle_{\text{post}}$ clearly separates from $\langle S_v \rangle_{\text{end}}$ (marked by a vertical light gray dashed line on figure 7). From figure 7b, we observed that net compaction is coincident with the emergence of a net particle lateral diffusion in the bed.

Figure 7c presents the ratio of $\langle S_v \rangle_{\text{end}} / \langle S_v \rangle_{\text{pre}}$ as a function of P_{drag}/P_0. Values above zero indicate hysteresis as, at the same Q_f, void sizes are statistically larger after local re-suspension has been established. We find some hysteresis ($\langle S_v \rangle_{\text{post}} / \langle S_v \rangle_{\text{pre}} > 0$) for discharge rates far under the critical value for maintaining cavities (vertical dashed line). Indeed, after a re-suspension episode, particles appear to always settle back to a more loose-packed state, as illustrated in photos of figure 3b, a nd fi gure 4d. However, it is noticeable that when the porous flow i s s trong e nough to cause bed compaction ($P_{drag}/P_0 > 0.04$), just as $\langle S_v \rangle_{\text{post}}$ decreases, $\langle S_v \rangle_{\text{post}} / \langle S_v \rangle_{\text{pre}}$ decreases, and then fluctuates a round a v alue of about 1.1 up to $P_{\text{drag}}/P_0 \simeq 0.06$.

For the range $0.06 \leq P_{\text{drag}}/P_0 \leq 0.064$, $\langle S_v \rangle_{\text{post}} / \langle S_v \rangle_{\text{pre}}$ increases rapidly to 1.2, as porous flow s tresses c an n ow m aintain some particles re-suspended in the post-stage of the experiment. At larger flow rate, this is followed by a decrease toward unity (i.e. there is no longer a hysteresis signature) as the flow becomes strong enough to trigger particle suspension during the pre-stage of the experiment.

4 Discussion

Using a novel apparatus, we have presented new results illustrating the small deformation induced at the particle scale as a sediment bed is traversed by a gentle porous flow. Our observations are obtained in a specific quasi-2D configuration, and the particles thus interact significantly with fixed solid walls. Yet, one can hypothesize that the channelization dynamics in the 2D case differs only quantitatively from the 3D case, similar to the Rayleigh-Taylor fluid dynamic instability, where faster initial growth in 3D

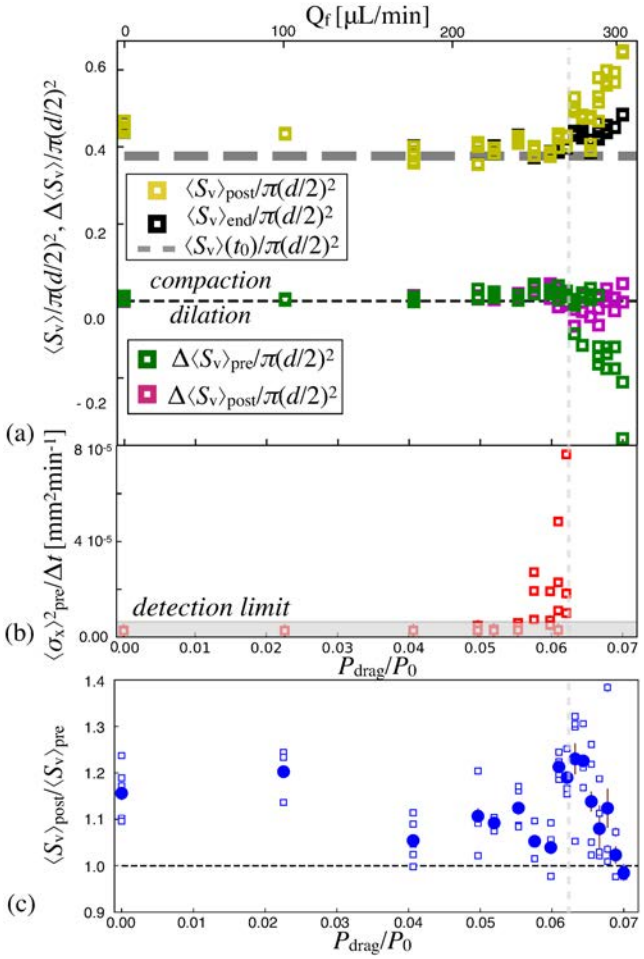

Fig. 7 (a) Yellow and black disks, respectively, represent the value of post-stage $\langle S_v \rangle_{\text{post}}$ and final stage $\langle S_v \rangle_{\text{end}}$ for each realization, as a function of the fluid drag force normalized by particle weight, P_{drag}/P_0. The thick gray dashed line represents the initial void size averaged over all the experiments, standard error being represented by the line thickness. Green and magenta squares respectively represent the difference of mean void size over the first 1000 seconds of the pre- and post-channelization stages of the experiments. Positive values indicate compaction during the pre-stage, while negative value indicates dilation of the system. (b) Standard deviation of particle lateral motion, averaged over 15 min and spatially, as a function of P_{drag}/P_0, for each realization. (c) Hysteresis measurement: ratio of mean void mean size during the pre- and post-stage of the experiments. Empty blue squares represent the values for each realization, and filled blue disks represent the average for fixed flow discharge Q_f.

is seen[27]. As each individual particle is surrounded by frictional particles in a quasi-2D random pack, the average number of contacts per particle should be similar to that observed for a pile of 2D disks, i.e. between 3 and 4. As the observed initial packing fraction is smaller than the classical 2D random packing fraction, we suspect our system geometry to have some effects on particle arrangement, making it slightly closer to a 3D packing. These hypotheses should be tested rigorously in future study. Regarding the wall effect on particles, they add similar frictional or viscous dissipation on each of the particles composing the bed. Therefore, there is an overall slowing of their dynamics in comparison with how particles would move in the middle of a 3D bed.

Our measurements of the void size distribution during the experiment show significant dynamics under low flow conditions: before a cavity can grow, net compaction occurs as an exponential decay in time of the void mean size toward a limiting value, in a way that may be similar to the compaction that dry granular beds undergo under tapping or vibration[28,29]. Interestingly, this similarity of slow compaction behaviors was recently observed in the case of sediment bed whose surface is sheared by a laminar fluid flow, at rates below the onset of sediment transport[30]. At the same time, particles exhibit a lateral effective diffusion, either individually as rattlers, or by collective rearrangements, both of which increase with the flow strength. Finally, over the range of fluid flow discharge where the hydromechanical instability leading to channeling and chimneys is triggered, we were able to quantify the net change of voids, and to show that this appears to occur in a discontinuous fashion, from net compaction to net dilation (green squares on figure 7a).

These observations prompt us to consider again the onset of fluidization in a disordered system of frictional particles. The concept of mechanical instability growth remains relevant to explain the development of localized deformation, either as a particular wavelength or as 'bubbles', as described for tall fluidized suspensions[31], or as a single chimney for low-aspect ratio jammed systems more similar to the one we have studied[18]. Yet, it appears that considering the bed as truly static and unable to deform plastically before the criterion of wavelength or cavity growth is incorrect, which has several important consequences. First, the jump from net compaction to net dilation may result from sensitivity of the dynamics to feedback from the small deformations of the bed, activated by the porous flow, to the flow resistance (and hence to the flow itself). Fluid flow stresses can clearly push particles close to the local criterion for motion. If motion results in bed compaction, statistically the number of frictional contacts per particle and hence the system rigidity must increase, but this is countered by the voids becoming smaller, so that the local flow velocity and thus the drag increase. The coincidence of these effects could explain the coexistence of beds exhibiting net compaction alongside channelization: a local flow strengthening due to compaction is a possible trigger for the growth of a mechanical instability.

The capacity for a dense bed to become more rigid with time at rest under the porous flow disturbance is also likely to play a part in the hysteretic behavior of a sediment bed near fluidization. More experimental and theoretical efforts, for example to visualize and model both networks of contact and flow field behavior

near critical, will be needed to further our understanding of these dynamics, which would help to predict long term evolution of sediment beds driven by fluid flows. Importantly, understanding mechanical details involved in the abrupt transition of void sizes could explain certain behaviors that to date are difficult to rationalize; these include unexpected clogging or the inverse (failure of clogged regions), and may contribute at their to understanding the onset of large-scale phenomena such as landslides and river channel formation or channel breaching[32,33]. Interestingly, our observations are consistent with recent observations of particle clogging dynamics in submerged silos, where it was found that vertical fluid flow could change the statistics of particle arrangements that are able to clog a silo[34].

Alternatively, if the porous flow is strong enough to cause slight particle rearrangement and make the bed compact, but not sufficient to destabilize it, the net effect of the porous flow is to consolidate the bed. This behavior may be dependent upon container geometry as well as tilt angles (below the angle of repose), as indicated by recent drum experiments made with frictional particles small enough to exhibit slight Brownian motion[35]. These lead us to conjecture that a weak flow that causes fluctuating forces on particles could result in slow flow, or creep, to gently 'anneal' the bed surface slope.

Finally, our study opens a new experimental field for study of mobile particulate beds. Microfluidic channels provide a highly controlled environment in which studies of phenomena ranging from clogging to precipitation or dissolution of soil components could be performed. Moreover, further miniaturization of this system, using particles in the range of $10^{-6} - 10^{-5}$ m, should allow close observation of the emergence of surface force effects between particles, and their impact on particles collective dynamics.

5 Conclusion

Using a novel 2D experimental model of a submerged sediment bed, the details of the particle dynamics near the onset of fluidization by a vertical liquid flow have been studied. As we are able to observe the well-known hysteretic behavior of the bed near the criterion for cavity growth into a chimney, we bring new results on the small change of the void dynamics over time, considering the behavior both before and after the system is dramatically changed by channel formation due to fluid flow and the resultant drag forces on the bed particles. For a certain range of flow discharge, the system can exhibit very different scenarios, where the bed can either exhibit small compaction due to the disturbance by the porous flow or strong dilation as it becomes channelized. These new results on one hand prompt consideration of the mechanism of bed compaction under weak porous flow conditions toward explanation of the hysteretic behavior, and on the other encourage the use of hard mobile particles in microfluidics studies of various pore-scale processes happening in sediments.

Conflicts of interest

There are no conflicts to declare.

Acknowledgements

Research was supported by the Levich Fellowship, from the City College of New York, to M. H.; partially by the National Science Foundation grant 1605283, to J. F. M.; and by the National Science Foundation grant CBET 1512358, to C. M. The authors thank Andrew Eng for technical assistance, and M. H. thanks Mark D. Shattuck and Joel Koplik for valuable discussions.

Notes and references

1 C. E. Stanley, G. Grossmann, X. C. i Solvas *et al.*, *Lab on a Chip*, 2016, **16**, 228–241.
2 R. Liefferink, A. Naillon, D. Bonn, M. Prat and N. Shahidzadeh, *Lab on a Chip*, 2018, **18**, 1094–1104.
3 E. Dressaire and A. Sauret, *Soft Matter*, 2017, **13**, 37–48.
4 J. J. Roering, J. W. Kirchner and W. E. Dietrich, *Water Resources Research*, 1999, **35**, 853–870.
5 W. E. Dietrich, D. G. Bellugi, L. S. Sklar, J. D. Stock, A. M. Heimsath and J. J. Roering, *Prediction in geomorphology*, 2003, 103–132.
6 S. S. Vyalov, *Rheological fundamentals of soil mechanics*, Elsevier, 1986.
7 J. K. a. Mitchell, *Fundamentals of soil behavior*, Wiley New York, 1993.
8 F. Boyer, E. Guazzelli and O. Pouliquen, *Phys. Rev. Lett.*, 2011, **107**, 188301.
9 R. Seto, R. Mari, J. F. Morris and M. M. Denn, *Physical review letters*, 2013, **111**, 218301.
10 M. Wyart and M. Cates, *Physical review letters*, 2014, **112**, 098302.
11 E. Brown and H. M. Jaeger, *Reports on Progress in Physics*, 2014, **77**, 046602.
12 A. Singh, R. Mari, M. M. Denn and J. F. Morris, *Journal of Rheology*, 2018, **62**, 457–468.
13 A. S. Keys, A. R. Abate, S. C. Glotzer and D. J. Durian, *Nature physics*, 2007, **3**, 260.
14 A. Kudrolli and X. Clotet, *Physical review letters*, 2016, **117**, 028001.
15 R. Jaeger, M. Mendoza and H. J. Herrmann, *Physical review letters*, 2017, **119**, 124501.
16 Y. Peng and L. Fan, *Chemical Engineering Science*, 1997, **52**, 2277–2290.
17 F. Zoueshtiagh and A. Merlen, *Physical review E*, 2007, **75**, 056313.
18 P. Philippe and M. Badiane, *Physical Review E*, 2013, **87**, 042206.
19 G. Ramos, G. Varas, J.-C. Géminard and V. Vidal, *Physical Review E*, 2015, **92**, 062210.
20 B. D. Gates, Q. Xu, M. Stewart, D. Ryan, C. G. Willson and G. M. Whitesides, *Chemical reviews*, 2005, **105**, 1171–1196.
21 I. Wong and C.-M. Ho, *Microfluidics and nanofluidics*, 2009, **7**, 291.
22 W. A. Beverloo, H. A. Leniger and J. Van de Velde, *Chemical engineering science*, 1961, **15**, 260–269.

23 K. To, P.-Y. Lai and H. Pak, *Physical review letters*, 2001, **86**, 71.

24

25 C. Cassar, M. Nicolas and O. Pouliquen, *Physics of fluids*, 2005, **17**, 103301.

26 M. Houssais, C. P. Ortiz, D. J. Durian and D. J. Jerolmack, *Physical Review E*, 2016, **94**, 062609.

27 N. Anuchina, V. Volkov, V. Gordeychuk, N. Es' kov, O. Ilyutina and O. Kozyrev, *Journal of computational and applied mathematics*, 2004, **168**, 11–20.

28 J. B. Knight, C. G. Fandrich, C. N. Lau, H. M. Jaeger and S. R. Nagel, *Physical review E*, 1995, **51**, 3957.

29 P. Richard, M. Nicodemi, R. Delannay, P. Ribiere and D. Bideau, *Nature materials*, 2005, **4**, 121.

30 B. Allen and A. Kudrolli, *Phys. Rev. Fluids*, 2018, **3**, 074305.

31 A. K. Didwania and G. M. Homsy, *International Journal of Multiphase Flow*, 1981, **7**, 563–580.

32 M. Houssais and D. J. Jerolmack, *Geomorphology*, 2017, **277**, 251–264.

33 A. Damsgaard, J. Suckale, J. A. Piotrowski, M. Houssais, M. R. Siegfried and H. A. Fricker, *Journal of Glaciology*, 2017, **63**, 1034–1048.

34 J. Koivisto and D. J. Durian, *Physical Review E*, 2017, **95**, 032904.

35 A. Bérut, O. Pouliquen and Y. Forterre, *arXiv preprint arXiv:1710.09111*, 2017.